Cross sections of electron excitation out of metastable helium levels with a fast metastable target produced via charge exchange

Mark E. Lagus, John B. Boffard, L. W. Anderson, and Chun C. Lin
Department of Physics, University of Wisconsin, Madison, Wisconsin, 53706
(Received 11 September 1995)

Absolute direct cross sections for electron excitation out of the 2 ^3S level and into the 3 ^3D, 4 ^3D, and 3 ^3S levels of the helium atom from threshold to 500 eV and into the 3 ^3P level over a more limited energy range have been measured using a fast metastable atomic beam target. We produce the metastable atoms via near-resonant charge exchange between a 1.6-keV He^+ ion beam and Cs vapor. Because this reaction is highly nonresonant with the ground state of helium, the charge-transfer process yields a primarily metastable beam. We use a thermal detector which we calibrate with ions to measure absolutely the neutral beam flux. The atomic beam is crossed by an electron beam, and we collect the resulting fluorescence at right angles to both the electron and atomic beams. We obtain the cross sections for excitation out of the 2 ^3S level into the various excited levels by monitoring the emission out of the excited level of interest.

PACS number(s): 34.80.Dp

I. INTRODUCTION

Electron excitation out of excited atoms into higher excited levels is a fundamental physical process that plays an important role in processes ranging from fluorescent lighting to gas discharge lasers to upper atmosphere dynamics. While electron excitation out of ground-level atoms has been studied for the past 80 years [1], experiments involving excited atoms require novel techniques and hence a comprehensive study of electron excitation out of excited levels has only recently begun [2,3].

Excited helium is a natural target candidate for electron excitation experiments. The two lowest-lying excited levels, the 2 ^1S and 2 ^3S levels, are both extremely long-lived metastable levels so that once they are produced, the atoms remain in the metastable levels until they collisionally deexcite (typically via collisions with the vacuum chamber). Electron excitation out of the ground level of He has been well studied and characterized [4,5] so that measurements of electron excitation cross sections out of the metastable levels of He allow one to compare excitation from excited levels to excitation out of the ground level. Furthermore, because helium is the simplest multielectron atom, it is the natural atom for comparing experimental measurements to theoretical calculations.

The study of electron excitation of metastable helium in our group began with the work of Rall *et al.*[6], who determined absolute apparent excitation cross sections out of the 2 ^3S metastable level and into the $n=3,4$ ^3S, 3 ^3P, and 3,4, 5,6 ^3D levels by the optical method, i.e., by measuring the intensity of the emission from the various n ^3L levels. Lockwood *et al.* [7,8] refined the apparatus and extended the measurements to the apparent excitation cross sections out of both the 2 ^1S and 2 ^3S levels and into the $n=3,4$ ^1S, 3,4 ^1P, and 3,4 ^1D levels.

These initial measurements reveal drastic differences between excitation out of the metastable levels and excitation out of the ground levels. In order to better understand these differences, Piech [9] has continued this first-generation experiment to fill in the gaps on the triplet side measuring (and in some cases remeasuring) cross sections out of the 2 ^3S into the $n=3,4,5$ ^3S, 2,3,4,5 ^3P, and 3,4,5 ^3D levels. The first-generation experiments, however, are limited to cross-section measurements from threshold (2.5–4 eV) to about 16 eV due to a high density of ground-level helium as detailed below.

Rall, Lockwood, Piech, *et al.* create the metastable atoms in a hollow cathode He discharge. This production method yields a metastable atom number density of about 10^8–10^9 atoms/cm^3. Most of the atoms, however, emerge from the hollow cathode in the 1^1S_0 ground state of helium (about 10^5 times more ground-state than metastable atoms). Even though the cross sections for electron excitation out of the ground state are about three orders of magnitude smaller than those for excitation out of the metastable levels, because of the unfavorable ground-state to metastable population ratio, once the electron energy is large enough to excite ground-state atoms, the signal from the ground-state excitation overwhelms the metastable excitation signal.

The threshold for excitation from the ground state occurs around 23 eV. However, in order to obtain optimum electron beam focusing and to collect correctly all of the incident electrons, they applied a positive bias to their Faraday cup. This, combined with the high-energy tail of the electron energy distribution, significantly lowered the apparent onset of ground-state excitation which, in practice, limited their experiments to electron energies below 16 eV.

To better understand excitation out of the He metastable levels, one must extend the measurements to much higher energies. In order to do this, one must have a metastable atom production method that yields metastable atoms without the overwhelming ground-state contamination. For this reason, in the present work, we describe an apparatus and display the results of an experiment that uses the charge-transfer process between fast He positive ions and Cs atoms via the reaction $He^+ + Cs \rightarrow He^*(2\ ^{1,3}S) + Cs^+$ to produce a metastable target with negligible ground-state contamination.

One understands metastable formation via charge ex-

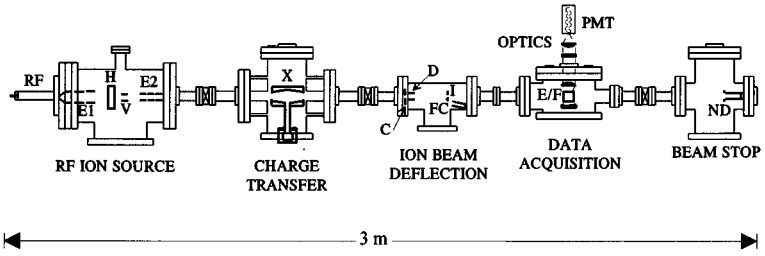

FIG. 1. Schematic diagram of the apparatus. rf ion source chamber: rf ion source (RF); Einzel lenses (E1, E2), and deflection plates (H,V). Charge-transfer chamber: charge-transfer cell (X). Ion beam deflection chamber: iris (I), collimation apertures (C), deflection plates (D), and off-line Faraday cup (FC). Data acquisition chamber: electron-gun–Faraday-cup setup (E/F), optics, PMT. Beam stop chamber: neutral detector (ND).

change from the perspective that, to the zeroth-order explanation, charge exchange is described by a parameter known as the energy defect ΔE which is simply the difference between the ionization energy of the donor atom (in this case Cs) and the binding energy of the receiving atom's (He) energy levels into which the electron transfers. Generally speaking, reactions that have small energy defects have large charge-transfer cross sections, and vice versa. The reaction $He^+ + Cs \rightarrow He + Cs^+$ is near resonant for the $n=2$ levels of He(ΔE range from -0.52 to 0.87 eV for the four $n=2$ levels) but highly nonresonant with the He ground state ($\Delta E = 20.69$ eV) so that at low collisional energies one expects the charge-exchange process to populate primarily the $n=2$ levels of He. Because of this, the main source for ground-state atoms in the neutral beam is production of atoms in the $2\ ^1P$ level since atoms in this level decay preferentially (with branching ratio 0.999) to the ground state.

Using a time-of-flight method, Reynaud *et al.* [10] found that the actual distribution of the populations among the $n=2$ levels involves a much more detailed explanation than one can obtain from an analysis based solely upon the energy defects and the statistical weights of the various He levels involved. In fact, this distribution depends upon both the alkali metal used and the incident ion energy [10,11]. Over the energy range 100–1250 eV, it is found that charge transfer from Cs to He^+ ions does not populate the $2\ ^1P$ level substantially. Therefore, unlike the first-generation experiment where a majority of the target atoms in the electron excitation region were in the ground state, one expects that most of the target He atoms formed via the charge-transfer process are metastable.

Hence by using a fast primarily metastable target we circumvent the limitations of the first-generation experiment imposed by the ground-state He contamination. This allows us to measure cross sections from excitation onset to arbitrarily high electron energy (in this case 500 eV). This paper describes our apparatus and presents our results for electron excitation out of the $2\ ^3S$ metastable level and into the $3\ ^3S$, $3\ ^3P$, $3\ ^3D$, and $4\ ^3D$ levels.

The target density in the fast beam is about 3×10^6 atoms/cm^3, much lower than the metastable density in the first-generation experiments ($\sim 5\times10^9$ cm^{-3}). We present much of this paper from the perspective of the steps that we take to optimize our signal rates and to overcome various noise sources in order to obtain electron excitation signal from the metastable levels of He.

II. EXPERIMENTAL APPARATUS

The apparatus has evolved into a beam line consisting of five chambers shown in block diagram form in Fig. 1. All chambers are pumped by 8-in. diffusion pumps using Santovac-5 pumping fluid. We equip each pump, with the exception of the one for the ion source chamber, with a refrigerated baffle. The background pressures range from about 10^{-7} Torr for the charge-transfer chamber to around 5×10^{-10} Torr for the data acquisition chamber (attainable after baking at 200°C for 48 h).

In addition to the radio frequency ion source, the first chamber also contains two Einzel lenses for beam focusing and horizontal and vertical deflection plates to steer the beam. The second chamber houses the charge-transfer cell where we partially convert the He^+ ions into metastable He atoms via the nearly resonant $He^+ + Cs \rightarrow He^+(2\ ^{1,3}S) + Cs^+$ charge-exchange process. The third chamber contains deflection plates and an off-line Faraday cup so that we can remove and monitor the remaining ions from the beam. This chamber also houses an iris which we can open and close via a rotary motion feedthrough, thus we can vary the diameter of the atomic beam at the position of the iris. We also need this chamber for differential pumping in order to handle the gas load from both the ion source and the charge-transfer chambers. The fourth chamber houses the electron gun and the data acquisition optics where we monitor the $He^*(2\ ^{1,3}S) + e^- \rightarrow He^*(n\ ^{1,3}L) + e^-$ process. The atomic beam is crossed by an electron beam, and we monitor the fluorescence at right angles to both the electron and atomic beams. During operation, the pressure in the data acquisition chamber (DAC) is usually less than 5×10^{-9} Torr. The final chamber contains our neutral detector.

A. Charge-exchange cell

The recirculating alkali-metal oven (Fig. 2) consists of three main parts: the charge-exchange region, the throat, and the reservoir. We chose to construct each part from stainless steel because of its high resistance to corrosion by alkali metals. The exchange region has entrance and exit apertures that allow passage for the beams of helium ions and atoms and an opening for the throat through which the cesium atoms enter. The exchange region's inner surface slopes down from the apertures to the throat opening.

The throat tube is welded between the exchange region and a flange that bolts to the reservoir. We insert into the throat a stainless steel mesh that extends from the exchange region opening to about an inch below the throat flange. Both the exchange region's slope and the mesh which acts as a wick facilitate the recirculation of the alkali metal.

We charge the reservoir with 20–25 g of Cs and bolt the oven together in an argon atmosphere. Cartridge heaters provide 200–600 W to the reservoir. Several type-K thermocouples monitor the temperatures. Refrigerated baffles on ei-

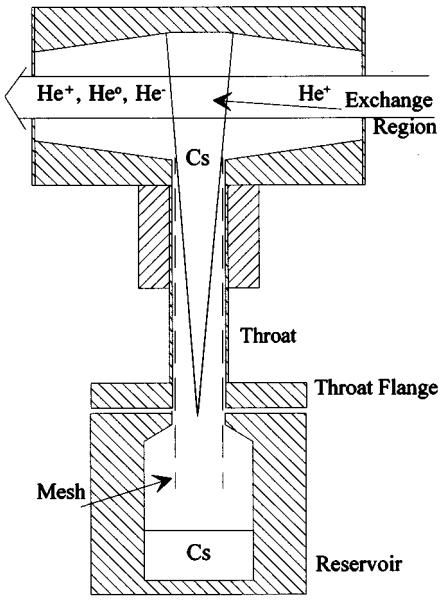

FIG. 2. Detail of charge-transfer cell.

ther side of the oven are chilled to $-40°C$ in order to condense the Cs that escapes the oven, thus reducing the contamination of the apparatus.

We heat the bottom reservoir which increases the alkali metal's vapor pressure. This creates a large pressure difference between the reservoir (at 260 °C) and the exchange region (at 50 °C), causing the atoms to travel through the throat and into the exchange region where the alkali-metal atoms interact with the helium ions. The exchange region temperature must remain above the alkali metal's melting point (30°C for Cs) for the oven to recirculate. Conduction from the reservoir delivers more heat to the top portion of the oven than is necessary so that we water cool copper blocks which are in good thermal contact with the top of the throat in order to keep the exchange region's temperature in the correct temperature range.

B. Electron gun

We acquire data using an electron gun with 11 stainless steel grids (Fig. 3). Standard BaO indirectly heated button cathodes are used because they offer high emission current density at relatively low temperatures (around 1000 K) [12].

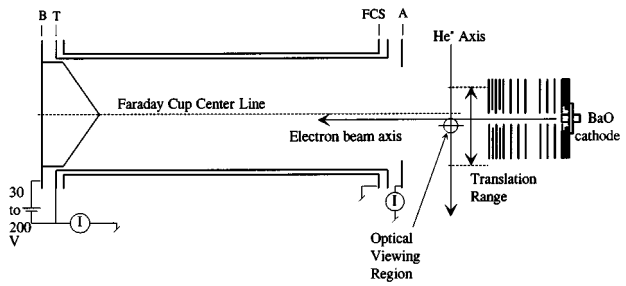

FIG. 3. Detail of translating electron gun Faraday cup assembly. *A*, aperture; *T*, Faraday cup tube; *B*, back plate; FCS, Faraday cup shield; *S*, gold blackened optical shield.

The cathode itself glows red to yellow hot, and the photomultiplier tube (PMT) receives significantly more blackbody radiation from the cathode than signal from electron excitation of metastable helium. Because of the extreme sensitivity to the cathode radiation, we have installed gold blackened shielding around the sides and back of the electron gun, and we gold blacken the gun's grids as well.

One special feature is that we mount the gun on a rack and pinion translation stage connected to a rotary motion feedthrough. This allows us to move the gun over a 2-cm range parallel to the axis of the metastable atom beam. We use this translation feature in a number of diagnostic tests, and it allows us to maximize the signal collected from excited levels of various lifetimes (see Sec. III A).

We collect the electrons with a Faraday cup assembly also shown in Fig. 3. It has three sections: aperture (A), Faraday cup tube (T), and back plate (B). The Faraday cup tube is encased by a grounded shield (FCS in Fig. 3) to prevent collection of stray thermal electrons. During operation, we monitor the electron current collected on the three sections A, T, and B.

The back plate is biased 30–50 V positive and is cone shaped to reduce the fraction of secondary and reflected electrons escaping from the Faraday cup. For the same reason, when acquiring data at high incident electron energies, we affix small permanent magnets to the exterior of the FCS with their poles perpendicular to the electron beam axis. The magnets and biased back plate are far enough from the collision region so that their fields do not penetrate into the data acquisition region. Diagnostic tests indicate that these measures eliminate the problems associated with secondary and reflected electrons generated within the Faraday cup assembly.

In order to ensure a field-free collision region and to further reduce the scattered light reaching our PMT, grounded gold blackened shields are installed on all four sides of the collision region. The plates above and below the electron beam have circular apertures, allowing us to detect the fluorescence from the He atoms. We cover these apertures with a coarse small gauge wire mesh. This prevents field penetration due to charge buildup on our optics' nonconducting surfaces. The metastable He beam passes through apertures on either side of the collision region.

In order to keep the electrons within the most efficient areas of our light gathering region, we first cancel the vertical and horizontal components of the earth's magnetic field with two Helmholtz pairs. We use a third Helmholtz pair to apply a 10–25 G collimating magnetic field along the electron beam axis.

C. Neutral detector

The primary components of the neutral detector include a back plate, a collection tube (4 cm diam$\times$10 cm length), and two entrance grids. This detector functions in three modes: as a secondary electron collector to monitor neutrals, as a Faraday cup to measure ions, and as a thermal detector to monitor either ions or neutrals. As a secondary electron collector, the back plate and entrance grids are biased negative, and we monitor the secondary electron current on the collection tube. In Faraday cup mode, the back plate and collection

tube are connected to an ammeter, while a negative bias voltage applied to the entrance grids suppresses secondary electrons.

The secondary electron current I_{ND} is used to measure the relative flux of He^+ atoms in the beam as data are collected. However, to determine the He^+ beam-particle current I_{He*} from the I_{ND} one must know the secondary electron ejection coefficient γ^*, which varies considerably with the surface conditions [13]. See Sec. IV A 4 for our method of measuring γ^*.

To determine the absolute He metastable flux, we use the detector in thermal mode [14]. The energy deposited onto the back plate per incident particle depends upon the kinetic energy of the particle rather than its species; each ion or metastable atom deposits 1.6 keV. Hence we determine the sensitivity of the detector by using an ion beam measured absolutely by the detector in Faraday cup mode. The back plate consists of a 25-μm polyvinylidene fluoride (PVDF) pyroelectric film held between two oxygen-free high-conductivity (OFHC) copper clamping flanges which act as heat sinks. As the He* (or He^+) heats the detector, the PVDF polymer deforms, moving charges to the aluminum electrodes on the front and back surfaces. The charge moved to the back surface is detected using a high-impedance field-effect transistor (FET) operational amplifier. By modulating the He* beam on and off the beam signal can be separated from thermal drifts and bias currents. While the back surface of the PVDF film is connected to the thermal detector circuitry, the front surface can be connected in the either the Faraday cup configuration or in the secondary electron collection mode.

D. Optics

An $f/0.93$ aspheric lens one focal length above the collision region and a concave mirror two focal lengths below are used to collect the fluorescence from the electron excitation process. The mirror increases the solid angle from which we gather photons, resulting in a 60% increase in signal. The light then passes through a 1-nm full width at half maximum (FWHM) narrow bandwidth interference filter which spectrally isolates the transition of interest. Finally, a $\frac{1}{2}\times$ magnification lens system images the viewing region onto the photocathode of our PMT. We use a Burle C31034A-02 GaAs PMT thermoelectrically cooled to $-30°$C in photon counting mode.

III. METHOD OF MEASUREMENT

In measuring electron excitation cross sections, two things interest us: the energy dependence of the excitation function, and the absolute magnitude of the cross section. The present section discusses how we measure the shape of the excitation functions. We present our method of absolute calibration in Sec. IV.

A. Acquisition of relative cross section

To measure relative cross sections for electron excitation out of the metastable levels of helium, we proceed in the following manner. The rf ion source produces a 1.6-keV ion beam with a measured energy spread of 40 eV (FWHM). Setting the charge-exchange oven temperature to approximately 250°C gives a Cs target thickness well within the single collision regime for converting the ions into metastable atoms. At the position of the electron beam the He* number density is approximately 3×10^6 atoms/cm^3. We monitor the metastable flux using the neutral detector in secondary electron collecting mode.

The 1.6-keV He atoms have a velocity of 2.77×10^7 cm/s. Most of the upper levels that interest us have lifetimes that range from 14 to 95 ns. Hence, in one lifetime, the excited atoms travel between 0.4 and 3 cm from the position where they are created before they decay. In order to maximize the signal, we translate the electron gun to a position upstream of the optical viewing region. The translation distance depends on the transition from which we collect the fluorescence.

All data are acquired with a 25-G magnetic field applied along the electron beam axis. The electron beam shows effects of space charge at low incident electron energies with an abrupt transition to non-space-charge-limited behavior at higher energies. The exact transition energy depends upon the voltages applied to the electron gun grids and can be set arbitrarily low. However, the magnitude of the electron current in the non-space-charge-limited regime increases with the transition energy so that to operate above the space-charge regime, and to maximize the signal rate, we acquire data using a variety of electron gun settings.

We have also found that the position of the electron beam's center is not constant for all energies. Evidence indicates that the shifting behavior results from a slight misalignment between the electron beam axis and the applied axial magnetic field (presumably due to slop in the translation stage). If ignored, the magnitude of the beam shift (<1 mm) is enough to introduce small (5–10 %) systematic distortions in the shape of the excitation functions. To account for this, we collect fluorescence at three or four gun positions that correspond to the position of the peak signal ±1 mm. At each gun position, we acquire data at three vertical positions of the fast beam (controlled by steering plates in the rf ion source chamber). The subsequent analysis of all the data averages out any effects of the shifting beam.

We typically take data 24 h a day. When obtaining data at a variety of electron energies, we cycle through the energies to eliminate any long time scale variations occurring over the duration of our data runs. it generally takes several weeks to obtain a single excitation function. The various parameters of operation (i.e., neutral detector response, atom beam focus and position, etc.) are reasonably stable and reproducible over a time period of weeks.

Because of the extremely small metastable number density and relatively large noise sources, we employ a double beam modulation strategy to extract the electron excitation of the He* signal. Amplified PMT pulses are fed into a discriminator. The large amount of rf noise generated by our ion source dictates that we set the discriminatory level at a relatively high level. A separate gating circuit modulates the electron beam on or off with a period of 1.6 ms. The circuit also generates two gates, A and B, both of 700 μs width. The A gate starts 70 μs after the electron beam is turned on, and the B gate starts 70 μs after the electron beam is turned off. The gates control two counters that are read into a computer. The fast (1.6 ms) modulation of the electron gun along

with the slow (100 s) modulation of the He* beam generates two pairs of counter readings—with the He* beam on ($A_{\rm on}$ and $B_{\rm on}$), and with the He* beam off ($A_{\rm off}$ and $B_{\rm off}$). The metastable electron excitation signal S_m is given by $S_m=(A_{\rm on}-B_{\rm on})-(A_{\rm off}-B_{\rm off})$.

B. Discussion of noise

For the purposes of our discussion, noise that registers as counts falls into four basic categories: dc sources (cathode light, rf noise, PMT dark current); sources that vary with the electron beam (electron-surface collisions, inelastic collisions with background gas atoms); noise that varies with the metastable beam (resonance light from metastable beam); and noise that varies with both the electron and the metastable beams (electron excitation of ground-state He atoms if the He partial pressure varies with the metastable beam). Because of the extremely thin metastable target, we assume that the He* beam's presence has no effect upon the electron beam. Hence our double beam modulation and subtraction schemes extract our signal from the first three categories of noise. We have had to take additional measures to eliminate the fourth category of noise.

Before the addition of metastable beam collimating apertures into the ion beam deflection chamber and prior to extension of the beam line to include the beam stop chamber, we used a quadrupole mass analyzer (QMA) to measure a He partial pressure in the data acquisition chamber that fluctuated in phase with the metastable beam. We ascribed this gas load to the large relatively uncollimated He* beam striking surfaces and collisionally deexciting within the chamber. We were also able to see electron excitation of ground-state atoms (despite the double subtraction) in our early excitation functions due to this fluctuating gas load. After installation of the beam collimating apertures and addition of the beam stop chamber, the QMA did not register the He partial pressure fluctuations, nor are we able to see ground-state contamination in our excitation functions.

By taking different combinations of the four counter readings we determine the size of the various noise sources in our experiment. As an example, consider electron excitation into the $3\,^3D$ level for which we observe the $3\,^3D\rightarrow 2\,^3P$ transition (587.6 nm). This line has the largest total signal due to its large cross section ($\sim 10^{16}$ cm^2), large branching ratio (1.00), short lifetime (14 ns), good filter transmission (55%), and good PMT quantum efficiency (20%). While the blackbody radiation is moderate at 587.6 nm, the fluorescence from the He* beam itself is a more serious problem. For typical He* and electron beam currents, we detect eight counts/s of actual electron excitation signal. In addition, we observe 1 count/s from light given off by the electron beam hitting surfaces in the collision region; 40 counts/s from scattered blackbody cathode light; and 900 count/s of light given off by the He* beam.

IV. ABSOLUTE CALIBRATION

Our method of absolute calibration is described in this section. First we derive the equation for finding the metastable cross section in terms of the known ground-state cross section. The subsequent four subsections describe several auxiliary experiments needed to find quantities needed in the absolute calibration. We then present the results of the absolute calibration along with an error analysis in Sec. IV B.

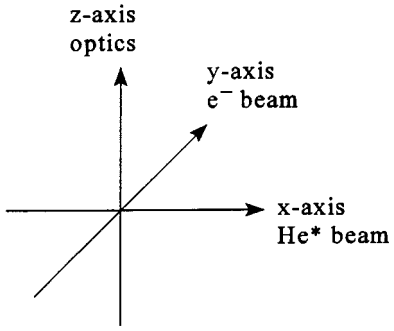

FIG. 4. Coordinate system. Y axis is into page.

A. Method

Consider a monoenergetic electron beam energetic enough to excite atoms from both the $2\,^3S$ metastable level and the ground state. We perform two experiments: one with a fast He* beam target, and one with a chamber filled with ground-state helium gas. The number of photons counted, S_m and S_g for the metastable and ground-state experiments, respectively, are

$$S_m=\xi Q_m\beta\Delta\int\Phi_f(\vec{r})n_m(\vec{r})[J(\vec{r})/e]d\vec{r} \tag{1}$$

and

$$S_g=\xi Q_g\beta\Delta'\int\Phi_s(\vec{r})n_g(\vec{r})[J'(\vec{r})/e]d\vec{r}, \tag{2}$$

where ξ is the total detector sensitivity (for optics and electronics), Q is the apparent cross section, β is the branching ratio, Δ the counter period, Φ is the probability of detecting a photon from an atom *excited* at position $\vec{r}$, n is the number density of targets at $\vec{r}$, J is the electron current density at $\vec{r}$, e is the absolute value of the electron charge, the primed quantities refer to the ground-state experiment, and the f and s subscripts refer to the fact that the metastable experiment is done with a fast beam, while the ground-state experiment uses a slow (thermal) target. By taking the ratio of these two signals we eliminate the unknown detector sensitivity; solving for the metastable cross section gives an expression for Q_m,

$$Q_m=Q_g\left(\frac{S_m/\Delta}{S_g/\Delta'}\right)\frac{\int\Phi_s(\vec{r})n_g(\vec{r})J'(\vec{r})d\vec{r}}{\int\Phi_f(\vec{r})n_m(\vec{r})J(\vec{r})d\vec{r}}. \tag{3}$$

In other words, we use the known cross section for excitation out of the ground level as part of our calibration. We define our coordinate system (Fig. 4) such that the He* beam is along the x axis, the electron beam is along the y axis, and the optics are on the z axis. Assuming that the beams have cylindrical symmetry about their respective axes of propagation over the size of the collision region, then each term in the integrals is only a function of two coordinates, e.g.,

$\Phi(\vec{r})=\Phi(x,y)$. We further assume that each function is separable, i.e., $\Phi(x,y)=\Phi(x)\Phi(y)$. These assumptions, which are exact in the case of Gaussian profiles, allow us to more readily calculate a final answer.

The $\Phi_{f,s}(\vec{r})$ functions are closely related to the optical profile of our viewing region. We define the optical profile function $\Omega(\vec{r})$ to be the relative probability of detecting a photon emitted at $\vec{r}$. In contrast, $\Phi_{f,s}(\vec{r})$ are defined to be the relative probability of detecting photons by atoms *excited* at position $\vec{r}$. The subscripts f and s remind us that the fast metastable atoms travel further from the position of the electron beam before they decay than do the slow ground-state atoms. Hence we write $\Phi_{f,s}(\vec{r})=\Omega(\vec{r}+\vec{v}_{f,s}T)$ where T is the time between excitation and decay of the atoms. Since a collection of excited atoms follows an exponential decay, T is not fixed for a given transition. The finer details of this point are addressed in the next section. Clearly, for thermal velocity atoms and excited states having lifetimes on the order of tens of nanoseconds, $\Omega(\vec{r}+\vec{v}_sT)\simeq\Omega(\vec{r})=\Omega(x)\Omega(y)$. Similarly we also neglect the transverse velocity in the fast beam. As a result, $\Omega(\vec{r}+\vec{v}_fT)\simeq\Omega(x+v_fT)\Omega(y)\equiv\Omega_f(x)\Omega(y)$.

The metastable number density for a beam of atoms moving with velocity v_f is $J_m(y,z)/v_f$, where J_m is the He* particle flux. We now define both the electron current density and the He* flux to have the form $J_{e,m}(u,v)=J^0_{e,m}j_{e,m}(u)j_{e,m}(v)$, where the j's are normalized profile functions, and J^0 is found from the condition that the integrated current density or flux equals the total current or particle current. We further assume that the profile of the electron beam is the same for the ground-state experiment and the metastable-state experiment. This is valid if the helium pressure is kept small ($<10^{-5}$ Torr). The integrals then become

$$\frac{\int\Omega_s(\vec{r})n_g(\vec{r})J'(\vec{r})d\vec{r}}{\int\Omega_f(\vec{r})n_m(\vec{r})J(\vec{r})d\vec{r}}=\frac{n_g}{(J^0_mv_f)}\left[\frac{J'^0_e}{J^0_e}\right]\left[\frac{\int\Omega(x)j_e(x)dx}{\int\Omega_f(x)j_e(x)dx}\right]\times\left[\frac{\int\Omega(y)dy}{\int\Omega(y)j_m(y)dy}\right]\times\left[\frac{\int j_e(z)dz}{\int j_e(z)j_m(z)dz}\right]. \quad (4)$$

Since the electron beams have the same profiles, the ratio of current densities J'^0_e/J^0_e equals the ratio of measured total current I'_e/I_e.

The integrals over x relate the overlap of where excited atoms are created to the optical detection efficiency at the point where the atoms decay. Using the model developed in the next section, we replace the x integrals with the calculated ratio (Ω_s/Ω_f). The next two sets of integral ratios depend upon the size of the He* beam. The ratio of y integrals compares the full size of the viewing region (as with a ground-state target) with the overlap of the He* beam and the optical efficiency. Likewise, the z integral ratio compares the width of the electron beam with the overlap of the electron and atom beams.

When we include the proper normalization conditions, we obtain the equation

$$Q_m=Q_g\left[\frac{S_m/\Delta}{S_g/\Delta'}\right]\left[\frac{I'_e}{I_e}\right]\left[\frac{\Omega_s}{\Omega_f}\right]\frac{n_g}{(I_{\mathrm{He}*}/ev_f)}\left[\int_{-\infty}^{\infty}j_m(y)dy\right]^2\times\left[\frac{\int_{-\infty}^{\infty}\Omega(y)dy}{\int_{-\infty}^{\infty}\Omega(y)j_m(y)dy}\right]\left[\frac{\int_{-\infty}^{\infty}j_e(z)dz}{\int_{-\infty}^{\infty}j_e(z)j_m(z)dz}\right]. \quad (5)$$

This equation requires two additional quantities to convert it into factors that are directly measured. First, we measure the partial pressure ΔP_{IG} of ground-state helium using an ion gauge. This is related to the *true* helium pressure by some correction factor K which accounts for the ion gauge's decreased sensitivity for helium. Using the ideal gas law we convert the pressure reading into a ground-state number density, $n_g=K\Delta P_{\mathrm{IG}}/kT$, where k is the Boltzmann constant and T is the temperature. Next, we note that we measure the secondary electron current from a mixed triplet-singlet metastable beam. Hence if the particle current of metastable atoms is (I_{ND}/γ^*), then the particle current of 2 ^3S helium atoms is $f_T(I_{ND}/\gamma^*)$, where f_T is the fraction of triplets in the beam. Upon substitution into Eq. (5) we obtain

$$Q_m=Q_g\left[\frac{S_m/\Delta}{S_g/\Delta'}\right]\left[\frac{I'_e}{I_e}\right]\left[\frac{\Omega_s}{\Omega_f}\right]\frac{\gamma^*\Delta P_{\mathrm{IG}}}{I_{ND}}\mathscr{C}_f, \quad (6)$$

where $\mathscr{C}_f$ represents a conversion factor which includes the various fixed numerical constants and the overlap integrals of the optics, electron beam, and atom beam,

$$\mathscr{C}_f=\left(\frac{K}{f_TkT}\right)ev_f\left[\int_{-\infty}^{\infty}j_m(y)dy\right]^2\left[\frac{\int_{-\infty}^{\infty}\Omega(y)dy}{\int_{-\infty}^{\infty}\Omega(y)j_m(y)dy}\right]\times\left[\frac{\int_{-\infty}^{\infty}j_e(z)dz}{\int_{-\infty}^{\infty}j_e(z)j_m(z)dz}\right]. \quad (7)$$

The quantities included in Eq. (6) (such as the electron current and gas pressure) vary from one data run to the next. The quantities included in the conversion factor, however, only vary slowly with time. Furthermore, $\mathscr{C}_f$ is independent of the transition being observed. Hence it needs to be determined only once.

1. Calculation of integrals over x

In the preceding section, we found that the integration over x (with a few minor alternations in notation) reduced to the ratio

$$\frac{\Omega_s}{\Omega_f}=\frac{\int\Omega(x)j_e(x;x_s)dx}{\int\Omega(x+v_fT)j_e(x;x_f)dx}, \quad (8)$$

where x is a variable corresponding to the position where the excited atoms are created. Since we move the electron gun to maximize the fast beam signal, x_s and x_f label the positions of the electron gun in the experiments with the slow and fast beams, respectively. From the form of this expression, one sees that this ratio depends upon the position of the electron beam, the velocity of the fast beam, and the lifetime of the excited level. In order to determine this ratio, we replace each integral with a double summation in the following man-

ner. Initially consider the signal collected from the fast beam excited by an electron beam centered at a position x_f. First we divide the electron beam profile along the x axis into slices of width Δx. The jth electron beam slice (centered at x_j) excites $N_j = C j_e(x_f)$ atoms in the target beam, where j_e is the profile of the electron current and C is some constant. Then, within any increment width Δx centered at x_i along the atom beam axis, a certain number of these atoms decay. The number of remaining excited atoms N_j^i entering the interval is equal to $N_j \exp[-(x_i - x_j)/v_f \tau]$, where τ is the lifetime of the excited state. One would expect the number of decays within the ith interval to be a product of N_j^i, the probability per unit time of decay which is the Einstein A for that transition A_{ul}, and the amount of time Δt required for the atom to traverse the length of one interval equal to $\Delta x / v_f$. The fraction of these photons that one actually detects depends upon where, relative to the peak of the Gaussian optical profile x_c, the decays occur. Hence the optical signal collected from the jth slice of the electron beam is simply

$$S_j(x_f) = \sum_i \frac{N_j^i A_{ul} \Delta x}{v_f} e^{(x_e - x_i)^2 / 2\sigma^2}, \tag{9}$$

where σ is the experimentally determined width of our Gaussian optical profile and x_i is the center of the ith interval (with x_i, x_c measured relative to our gun's initial position x_f).

We then sum over all of the slices of the electron beam to obtain the total signal from the fast beam,

$$\Omega_f(x_f) = \sum_j S_j(x_f). \tag{10}$$

We obtain a similar expression for the total signal from the slow beam $\Omega_s(x_s)$ via the identical procedure.

These summations entail straightforward numerical calculations that we have performed. The absolute magnitudes of the profiles $\Omega_{s,f}$ are set by the arbitrary constant C, however, we are only interested in the shape of the profiles. In Fig. 5, we plot the normalized profiles $\Omega_s(x)$ for thermal velocity atoms and $\Omega_f(x)$ for a fast beam using two different lifetimes for the fast beam. One sees that the peak in the fast atomic beam signal occurs at electron gun positions significantly upstream of the optical axis whereas the excitation from the thermal velocity atoms has maximum signal directly beneath the optics ($x_s = 0$). The calculations also show that, as expected, the signal maxima for the fast beam occur at upstream distances that increase with the excited-state lifetime.

Because we can also translate the electron gun over a 2-cm range along the metastable beam axis, we can directly measure the profiles $\Omega_f(x)$ and $\Omega_s(x)$ as a function of electron gun positions (as described in Sec. IV A 2). The results in Fig. 6 show good agreement between the measured and calculated profiles.

We use our calculation to determine the ratio $[\Omega_s(x_s)/\Omega_f(x_f)]$. For example, the 5876-Å line has a 14-ns lifetime. For a gun position centered beneath the optical axis ($x_s = x_f = 0$), $\Omega_s(0) = 1.0$ and $\Omega_f(0) = 0.51$. In actuality, we perform the absolute calibration at a variety of electron gun positions (x_s not necessarily equal to x_f) and use the appropriate values for Ω_s and Ω_f.

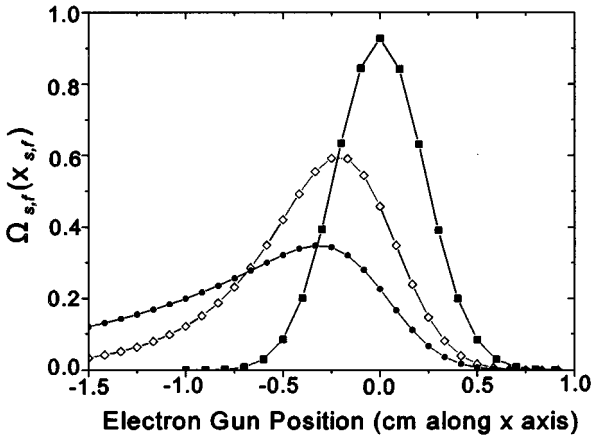

FIG. 5. Calculated profiles for a thermal beam with excited-state lifetime of 14 ns (■), and two fast beams (1.6 keV) with excited-state lifetimes of 14 ns (◇) and 36 ns (●).

2. Determination of profile functions

In practice, the most difficult step in our absolute calibration procedure is the accurate determination of profile functions for the optics, electron beam, and metastable beam. For the optical profile we fill the chamber with gas and record the signal as we translate the electron gun across the viewing region. To obtain profiles for the electron and metastable beams, we employ the rotating wire apparatus (Fig. 7), which consists of a rotary motion feedthrough electrically separated from the chamber by a ceramic break. On the end of the feedthrough is a bent 0.010-in. tungsten wire which rotates in a circle of 16.5 mm diameter. When the neutral beam strikes the wire, secondary electrons are ejected. We determine the neural beam profile by measuring the secondary electron current as a function of wire position.

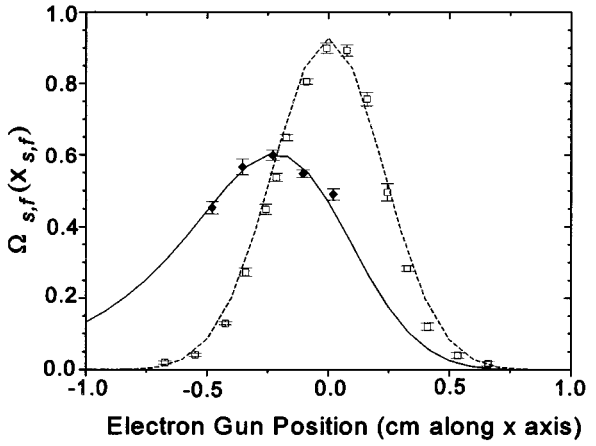

FIG. 6. Comparison between calculated and measured profiles for fast (◆, $2\ ^3S \rightarrow 3\ ^3D$) and slow (□, $1\ ^1S \rightarrow 3\ ^3D$) targets. Data are normalized to calculations (lines) at peaks.

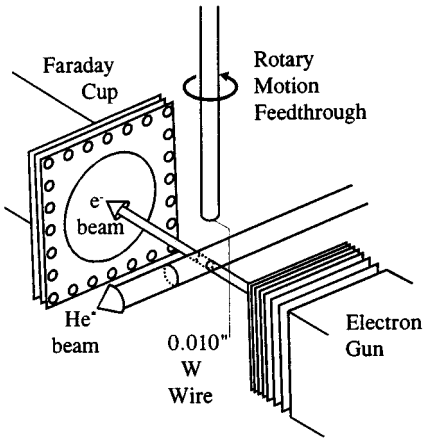

FIG. 7. Schematic diagram of rotating wire assembly.

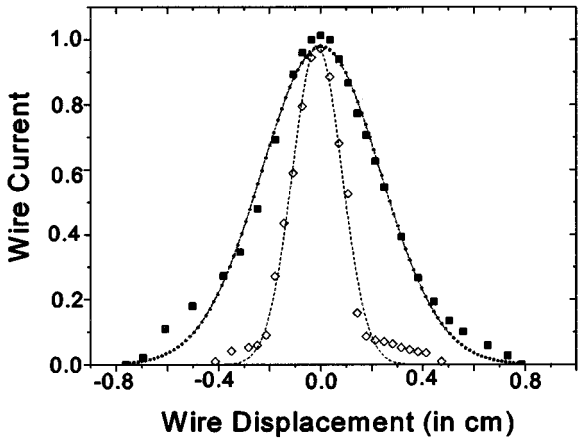

FIG. 8. Profiles of electron beam (◇) and neutral beam (■) obtained from rotating wire apparatus.

By directly measuring the current on the wire as a function of wire position, the same apparatus is used to find the electron current distribution. The measured current on the wire actually consists of the incident electron current minus the secondary electron current. Because the secondary electron current is proportional to the incident electron current, secondary electrons do not affect the shape of the electron current distribution. Furthermore, while the presence of the wire does not disturb a neutral beam, one may question whether the wire affects an electron beam. This concern does not appear to be a serious problem; biasing the wire by ± 2 V does not change the profile.

A 360° rotation of the wire yields two profiles for each beam. The difference between the profiles gives an indication of the spread of the beams as they propagate. The two neutral beam profiles are functionally identical (as one would expect for a collimated beam) so that we may use either profile as the distribution at the collision region. Both electron beam profiles are well approximated by Gaussians, but the Gaussian on the far side of the collision region is significantly wider than the one nearest the electron gun. Therefore we assume that the profile at the center is a Gaussian having a FWHM which is the average of the FWHM of the far- and near-side profiles. Furthermore, the fact that all of the profiles (see Fig. 8) are well approximated by Gaussians lends credence to the separation of variables step employed in the derivation of cross-section formulation.

3. Determination of ground-state He number density

We perform the ground-state helium experiment in a flowing mode. By increasing helium flow into the system at the position of the ion source and by closing various combinations of gate valves along the beam line, we can raise the partial pressure of helium within the DAC to arbitrarily high values. We then record the difference in the pressure reading ΔP_{IG} of an ion gauge mounted in the chamber with the helium flow on and off.

In order to calibrate our ion gauge for helium, we temporarily installed an MKS Type 120AA Baratron Vacuum Gauge onto the side arm in close proximity with the ion gauge. This baratron has a quoted resolution of 10^{-6} of its 0.1 Torr, but output voltage fluctuations limited our measurements to above 5×10^{-6} Torr. It also has a recent absolute calibration traceable to the National Institute of Standards and Technology. Because we typically perform the ground-state helium experiment at helium partial pressures below 10^{-6} Torr, calibration of the ion gauge in the lowest pressure range required two steps. First, over the range of pressures where the baratron is calibrated (from 10^{-6} to 10^{-3} Torr), we determined that the ion gauge reading is proportional to the output of the baratron with a correction factor K equal to 10.0. The factor K includes both the fact that the helium ionization rate is smaller than the ionization rate for air and the systematic inaccuracy of the ion gauge's response. Second, beginning with the lowest He partial pressures ($\sim 2\times10^{-7}$ Torr) and extending well into the baratron gauge range ($\sim 5\times10^{-5}$ Torr), we determined that the amount of electron excitation signal out of the ground state was proportional to the pressure which we measured with the ion gauge. These two steps demonstrate that the pressure measured by the ionization gauge is linear over four orders of magnitude and that we obtain the absolute He partial pressure by multiplying the partial pressure obtained from our ion gauge by the correction factor for He (10.0 ± 0.5).

4. Determination of γ^*

Two steps were employed in determining γ^*. The first step is to determine the sensitivity of the thermal detector. By applying a modulation voltage to the set of deflection plates in the beam deflection chamber, we modulate the ion beam component remaining in the charge-exchanged fast beam. Using the detector in Faraday cup mode, we measure the absolute ion current incident upon the detector. We simultaneously record the voltage output from the charge-sensitive amplifier connected to the back surface of the PVDF film. This voltage signal is proportional to the heat absorbed by the film in the 30-s modulation period. The ratio of these two signals determines the detector sensitivity η, expressed in V/μA for 1.6-keV particles (for a fixed 30-s modulation period). We have verified that η is constant for beam currents from 0.1 to 10 μA.

We next use the thermal detector to measure the He* particle current. To do this, we first deflect the ions remaining in the charge-exchanged beam, leaving us with only

metastable atoms. Next, the modulation voltage is applied to a set of deflection plates in front of the charge-exchange cell; this modulates the He* beam on and off. We now use the voltage output of the thermal detector along with the value of η found from the ion measurement to determine $I_{\mathrm{He}*}$. Finally, γ^* is found from the ratio of secondary electron current to calculated He* particle current. We measure γ^* before each data collection run using the same ion beam focusing as used in the data run.

5. Triplet fraction, f_T

The fraction of 2 ^3S He atoms in the fast beam primarily depends upon two factors: the fraction of the ions that undergo charge exchange with Cs and end up in the 2 ^3S level, and how much of the ion beam is neutralized by collisions with background gas. For 1.0-keV He^+ incident on cesium, Reynaud *et al.* have measured $f_T = 0.72$ [10]. At higher energies one expects this to approach the statistical weight of $\frac{3}{4}$. The triplet fraction in our beam is slightly less than this value because a finite number of the ions undergo resonant exchange with the residual helium gas before the ions reach the charge-transfer cell. Most of this resonant neutralization occurs upstream of the deflection plates that modulate the signal so that this contribution is a dc noise source that gets subtracted off in the data analysis. Nevertheless, from the background pressure in the ion source chamber, the resonant charge-exchange cross section, and the path length of the ions, we estimate that less than 2% of the ion beam is converted into ground-state helium due to resonant charge exchange between the deflection plates and the charge-transfer cell. Allowing for these effects, we estimate f_T is equal to 0.70 ± 0.03.

B. Results and analysis of uncertainties

The first step in the calculation of absolute cross section is the determination of the conversion factor $\mathscr{C}_f$. Once the value of $\mathscr{C}_f$ is known, it is a simple matter to find the value of the absolute cross section from Eq. (6).

Two sets of quantities are needed to find $\mathscr{C}_f$: a number of numerical constants (such as the electron charge and the beam velocity), and profile functions for the optics, electron beam, and atom beam. We combine the numerical constants and numerically integrate the profiles to obtain a value for $\mathscr{C}_f$.

The value of $\mathscr{C}_f$ depends strongly upon the ion beam focus conditions which determine the neutral beam profile. However, it is only weakly dependent upon the electron beam and optical profiles. For example, changing the electron beam width by 20% yields a 5% change in $\mathscr{C}_f$. Similarly, changing the Gaussian profile of the electron beam to a square profile causes only a 5% change. This is in contrast to a 10% random variation in the answer from using different metastable beam profiles taken with the same ion beam focusing. Combining this 10% uncertainty in quadrature with estimates for the other sources of uncertainty (5% each for the optics and electron gun profiles, 3% for beam velocity, 10% for the temperature, 5% for each for the ion gauge correction and triplet fraction), the total uncertainty in $\mathscr{C}_f$ is estimated to be on the order of 20%.

Additional uncertainties contribute to the total uncertainty in Q_m. The ratio (Ω_s/Ω_f) depends on the optical and electron gun profiles, and as a result has about a 5% uncertainty. We measure the secondary electron emission coefficient γ^* to about 10% uncertainty, while the statistical uncertainty in the metastable signal ranges from 5% to 15% depending on the transition. The remaining values used to find the ratio of the metastable cross section to ground-state cross section have negligible uncertainty ($<3\%$) since they rely only on the linearity of the measuring device. For the ground-state excitation cross sections we use the values of Ref. [4].

V. RESULTS AND DISCUSSION

A. Absolute results

We perform the absolute calibration experiment at one electron energy that corresponds to the peak of the ground-state cross section (27 eV). We then use our relative excitation functions to obtain the absolute cross section at all energies. As a check of the robustness of our method we have performed the calibration experiment at different electron gun focus conditions and gun positions. The present work reports absolute apparent cross sections from the 2 ^3S metastable level into four higher-lying excited levels: the $n=3$ ^3S, ^3P, and ^3D levels and the 4 ^3D level.

1. Cascade contributions

We measure apparent cross sections which are the sum of the direct excitation cross sections and cascades from higher levels. However, in the case of our fast beam target, the apparent and direct cross sections are nearly identical in contrast to the static target experiments. This occurs because photons that correspond to cascade contributions to our signal result from a minimum of two decays (one from the higher-lying level into our level of interest and the subsequent decay that we detect) whereas the photons resulting from direct electron excitation only require one decay. For example, the primary cascade contributions into the S and D levels are from the P levels. The lifetimes of the 3, 4, and 5 ^3P levels (95, 154, and 234 ns) translate into one lifetime flight distances of 3, 4.5, and 7 cm, respectively. Most of the atoms excited into these levels do not decay into our levels of interest until they travel beyond the viewing region.

We quantitatively estimate the reduction of the cascade contributions to our absolute cross sections due to the fast motion of the target beam using a method similar to the one used to evaluate the integrals over x (Sec. IV A 1). For example, the first-generation experiment estimates that at 10 eV, 10% of their 3 ^3S level apparent cross section is due to cascades [9]. We estimate that only around 1% of our 3 ^3S cross section at 10 eV and 2% at 200 eV is due to cascades.

Our 3 ^3D cross-section measurement is virtually free of cascades from the n ^3P levels. The cross sections into the n ^3F levels are unknown, but they are presumed to be small. From this, and because of their relatively long lifetimes (72 and 138 ns for the $n=4$ and 5 levels), we assume cascades from the n ^3F levels do not appreciably contribute to the apparent cross section.

Of the cross sections that we report, the 3 ^3P apparent cross section contains the largest cascade contributions to its

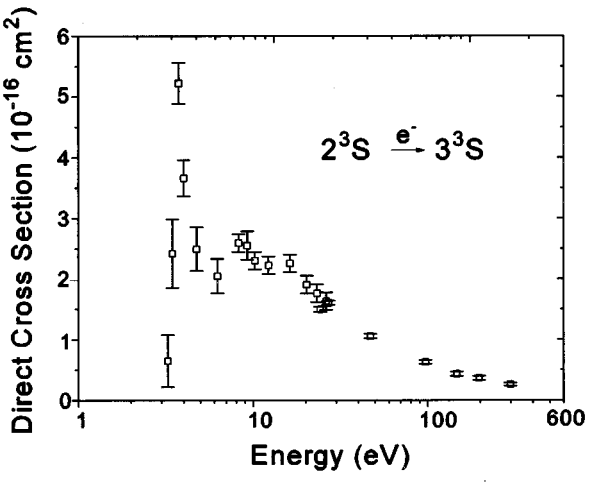

FIG. 9. Direct cross section for excitation into the 3 ^3S level. The error bars indicate statistical error only, and do not include the systematic uncertainty of the absolute calibration.

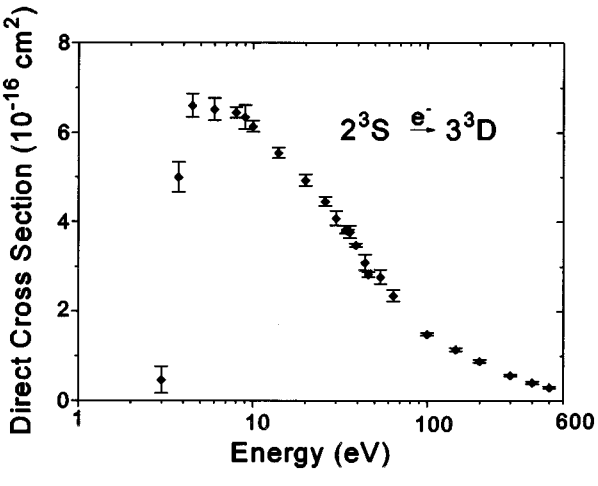

FIG. 10. Direct cross section for excitation into the 3 ^3D level. The error bars indicate statistical error only, and do not include the systematic uncertainty of the absolute calibration.

value. We estimate that at 27 eV about 10% of its value is due to cascades.

Since the apparent cross sections obtained in this paper differ from the apparent cross section as defined in conventional usage, we do not present these data directly to avoid confusion. We apply the estimated cascade corrections as indicated above, and show the direct excitation cross sections in the succeeding sections.

2. Absolute cross sections

Figures 9 and 10 display the direct excitation cross sections from threshold to 500 eV for excitation into the 3 ^3D level and to 300 eV for excitation into the 3 ^3S level. The data include statistical error bars that do not reflect the overall 35% systematic uncertainty of our calibration method. Table I lists our results at a number of different energies for excitation into the 3 ^3S, 3 ^3P, 3 ^3D, and 4 ^3D levels. Due to the long lifetime of the 3 ^3P level (95 ns) and low filter transmission at short wavelengths, we have only taken a limited amount of data for excitation into the 3 ^3P level.

B. Systematic effects

1. Polarization

We have neglected polarization effects. Allowing for polarization of both the metastable and ground-state signals, our values need the additional correction

$$\bar{Q}_m(E) = Q_m(E)\left[\frac{1-\langle P_m(E)\rangle/3}{1-\langle P_g\rangle/3}\right], \tag{11}$$

where $\bar{Q}_m$ is the cross section corrected for polarization, Q_m is the uncorrected cross section, and P_m and P_g are the polarization fractions of the metastable and ground-state signals averaged over the solid angle that light is collected from. We include the electron energy E explicitly to emphasize that the metastable polarization represents an excitation function shape distortion effect while the ground-state polarization represents a shift in the magnitude of the cross section.

While the polarization of light emitted from excitation of ground-state atoms P_g is generally known, no previous measurements have been made for metastable excitation. We

TABLE I. Direct cross sections for excitation from 2 ^3S to n ^3L states. All cross sections are in units of 10^{-16} cm^2. Error bars are for 35% uncertainty in absolute calibration.

Incident energy	Q_d (10^{-16} cm^2)			
(eV)	3 ^3S	3 ^3P	3 ^3D	4 ^3D
3.5	8.1 ± 2.8		5.1 ± 1.8	
6	2.2 ± 0.9		6.7 ± 2.3	1.0±0.4
10	2.5 ± 0.7	1.6±0.7	6.3 ± 2.2	1.1±0.31
16	2.2 ± 0.8		5.4 ± 1.9	0.93±0.33
27	1.6 ± 0.6	1.2±0.4	4.5 ± 1.6	0.75±0.26
40	1.2 ± 0.4		3.5 ± 1.2	0.63±0.22
50	1.0 ± 0.35		2.9 ± 1.0	0.56±0.20
100	0.61 ± 0.21		1.5 ± 0.5	0.25±0.09
200	0.36 ± 0.13		0.90 ± 0.31	
500	0.16 ± 0.06		0.30 ± 0.11	

TABLE II. Comparison of experimental cross-section results at 10 eV. The results from this experiment and those of Piech are direct cross sections. Results from Refs. [17,18] are level cross sections that have not been corrected for cascades. All cross sections are in units of 10^{-16} cm^2.

Level	This expt.	Piech [9]	Mityureva and Penkin (1989) [17]	Gostev *et al.* [a] (1980) [18]
$3\ ^3S$	2.5	3.9		
$3\ ^3P$	1.6	2.2	120	2
$3\ ^3D$	6.3	9.5		8.5
$4\ ^3D$	1.1	1.7	45	0.7

[a]The excitation functions of [18] are drastically different from our results. Comparison at most energies other than 10 eV would show a much larger discrepancy.

have not measured the metastable polarization because of the small signal rates associated with our apparatus. However, based on reasonable estimates of the polarization fractions, we still expect this to be a minor ($\ll 10\%$) correction to most of our results. The $3\ ^3S$ level should need no correction at all.

As an example, consider the theoretical results of Flannery and McCann [15] for polarization of the fluorescence from the $3\ ^3D$ level. The theory predicts the polarization fraction varies from 0.175 near threshold to -0.072 at 100 eV with the zero crossing between 20 and 50 eV. These results would suggest that we may underestimate the cross section at high energy by about 2.5% and overestimate the cross section by 6% near threshold. Both of these corrections seem negligible in light of our statistical uncertainty. Since our absolute calibration experiment is done at 27 eV, near the zero of the polarization fraction calculation, it should be completely free of polarization corrections.

2. Contribution from non−2 ^3S levels

We estimate the fast beam fractions of the $2\ ^1S$ metastable level and 1^1S ground level to be 0.20 and 0.10, respectively. In this section, we consider the effect of fluorescence from these levels upon our cross-section measurement.

Cross sections for excitation from the ground state are smaller than those for excitation of the metastable levels by two to three orders of magnitude over the entire energy range. Hence, signal from fast ground-state atoms represents a negligible correction to our measurements.

Excitation cross sections from the $2\ ^1S$ into the $n\ ^3L$ levels have not been measured. For excitation out of the ground level the spin-forbidden excitation ($1^1S \rightarrow n\ ^3L$) cross sections decrease with energy much more rapidly than do the spin-conserving excitation ($1^1S \rightarrow n\ ^1L$) cross sections, but the peak cross sections are in some cases comparable [4]. Lockwood *et al.* [7], however, showed that the peak $2\ ^3S \rightarrow n\ ^1L$ cross sections are several times smaller than the peak $2\ ^1S \rightarrow n\ ^1L$ cross sections. For excitation into triplet levels ($n\ ^3L$), theoretical calculations predict the peak magnitudes of the spin-exchange and spin-conserving cross sections may be comparable [16]. Taking these three sets of comparisons together, we estimate that the singlet fraction in the fast beam could lead to as much as a 10% correction to our values near excitation threshold but almost no correction at higher energies. Because we do not know the magnitudes of the $2\ ^1S \rightarrow n\ ^3L$ cross section, we have not attempted to correct for excitation from the $2\ ^1S$ level.

C. Comparison to previous experiments

Table II lists our results along with the direct cross sections of the first-generation experiment at 10 eV. Although the latter are substantially larger than the former, the two sets of cross sections overlap within their margins of uncertainty. It is interesting to note that the ratios of the cross sections ($3\ ^3D$:$3\ ^3S$:$3\ ^3P$:$4\ ^3D$) at 10 eV for our results (1:0.39:0.26:0.17) show excellent agreement with the first-generation experiment (1:0.41:0.23:0.18). Furthermore, while the two experiments disagree in magnitude, we obtain virtually identical excitation function shapes in the energy regime where the two experiments overlap.

The authors are aware of only two additional absolute measurements of the integral excitation cross section for helium metastable atoms. Both have been limited to energies less than the ground-state threshold. Values for apparent cross section at 10 eV for each experiment are also given in Table II.

The experiment of Mityureva and Penkin [17] uses a low-pressure (100 mTorr) discharge to produce metastable helium atoms. Their results are much larger than the values we have measured. Furthermore, they indicate that the cross sections for both the $3\ ^3P$ and $4\ ^3D$ are larger than the cross section for $3\ ^3D$ in contradiction to both this experiment and theoretical predictions.

Gostev *et al.* [18] used a fast metastable beam formed by resonant neutralization of a helium ion beam with a solid converter. Our results would seem to compare favorably with their values at 10 eV. However, their excitation functions are drastically different from ours. For example, the ratio of the $3\ ^3D$ peak cross section to the value at 10 eV is approximately 12 in their experiment, while our ratio is about 1.1. Hence a comparison at just about any other energy would lead to large discrepancy between our results and theirs.

D. Comparison to theory

Calculations of the electron-impact excitation cross sections out of the $2\ ^3S$ level into the $n\ ^3L$ levels with n from 2 to 5 by means of the Born approximation have been reported by Ton-That, Manson, and Flannery [19]. Kim and Inokuti [20] have also given Born cross sections for the $2\ ^3S \rightarrow 3\ ^3D$ excitation and their values are in good agreement with those of Ton-That, Manson, and Flannery. In Fig.

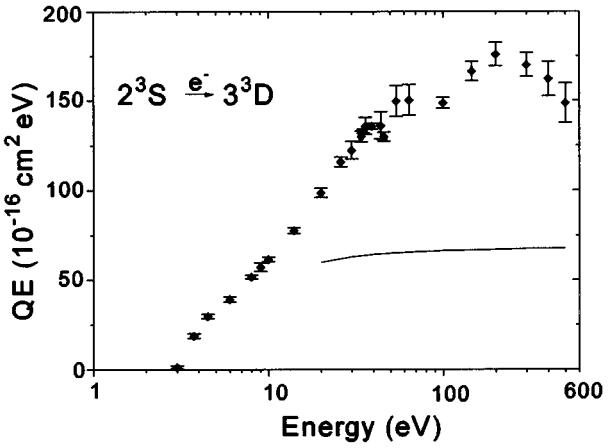

FIG. 11. Bethe plot for excitation into the 3 ^3D level compared to Born theory calculations of Ton-That, Manson, and Flannery [19] (solid line). The error bars indicate statistical error only, and do not include the systematic uncertainty of the absolute calibration.

11 we compare the measured 2 $^3S \rightarrow 3\ ^3D$ excitation cross sections with Born values in a Bethe plot of energy times the cross section versus log$E$. For an excitation corresponding to an optical quadrupole transition the Born cross sections behaves like E^{-1} at the high-energy limit (evident in Fig. 11 as a flat line). The experimental values of EQ, however, increase until about 200 eV, and then show a slight decline. Clearly the cross sections have not yet reached the high-energy Born regime at 500 eV. To examine the Born-Bethe behavior it is necessary to measure the cross sections at energies much higher than 500 eV. This poses an experimental problem since cross sections decrease with energy and the signal becomes very weak. For the 2 $^3S \rightarrow 3\ ^3S$ excitation we have measured the cross section up 300 eV. At this energy the Bethe plot (not shown) is still rising and the measured cross section is much larger than the Born value.

At lower energies cross sections for the 2 $^3S \rightarrow n\ ^3L$ excitations have been calculated using a variety of different methods: the multichannel eikonal theory (MET) [15], the R-matrix method (RMM) [16], the distorted-wave approximation (DWA) [21], the updated multichannel eikonal theory (DMET) [22], two versions of the first-order many-body theory (FOMBT) [23], and the convergent close-coupling (CCC) method [24]. Selected theoretical cross sections for the 3 ^3S and 3 ^3D levels from the various methods are shown in Table III along with our experimental values. Here we obtain the RMM and DMET cross sections by reading from the plots given in the original papers and obtain the DWA cross section at 31 eV by interpolating between 23 and 33 eV (after conversion to incident energy). The MET calculation covers five energies from 5 to 100 eV, but we find the difference in cross section between two adjacent energies too large to interpolate for inclusion in Table III. A visual display of the comparison of the experimental values of the present work and of Refs. [9,18] with the various theoretical calculations for the 3 ^3D and 3 ^3S levels are shown in Figs. 12 and 13, respectively. The curves for the theoretical cross sections for these figures are obtained by joining cross-section values taken out of tables given in the original papers or at various energies directly off of the curves given in the original papers.

The RMM values show very good agreement with our results in both shape and magnitude. The DWA cross section for 3 ^3S in the energy range of 13–23 eV (not included in Table III) also agrees well with our measurement. Although both MET and DMET give cross sections smaller than ours, the general energy dependence of the 3 ^3D cross section from these two methods is consistent with our data. The FOMBT cross sections are larger than ours at 6 eV and smaller than ours at 16 eV. The CCC method, which has provided differential cross sections for excitation out of the *ground level* of He into various excited levels [25] in beautiful agreement with experiments, gives cross sections about one-half of our experimental values for excitation out of the 2 ^3S metastable levels into the 3 ^3S and 3 ^3D levels. In this regard it is interesting to note that the CCC values of the ionization cross sections of the metastable He atom are also smaller than the experimental values of Ref. [26] by approximately a factor of 2 and that the differential cross sections for excitation out of the 2 ^3S level calculated by the CCC method are likewise significantly below the experimental values of Ref. [27]. In contrast the DWA and FOMBT show reasonable agreement with the experimental differential

TABLE III. Comparison of the experimental cross sections for excitation out of the 2 ^3S level into the 3 ^3S and 3 ^3D levels with theoretical values. See Sec. V for details concerning the calculations and sources of the numbers quoted.

		Theory						
E (eV)	This expt.	RMM	MET	DMET	DWA	FOMBT(1)	FOMBT(2)	CCC
				2 $^3S \rightarrow 3\ ^3S$ excitation				
6	2.2	2.8		0.94		5.90	7.70	
10	2.5	2.1	1.51	1.0		2.58	3.01	
16	2.2			0.94		1.75	1.86	1.20
31	1.6			0.71	1.1			0.779
				2 $^3S \rightarrow 3\ ^3D$ excitation				
6	6.7	6.7		5.1		18.76	24.20	
10	6.3	6.0	5.56	5.6		5.48	6.40	
16	5.4			4.2		3.51	3.73	2.85
31	4.1			2.7				2.04

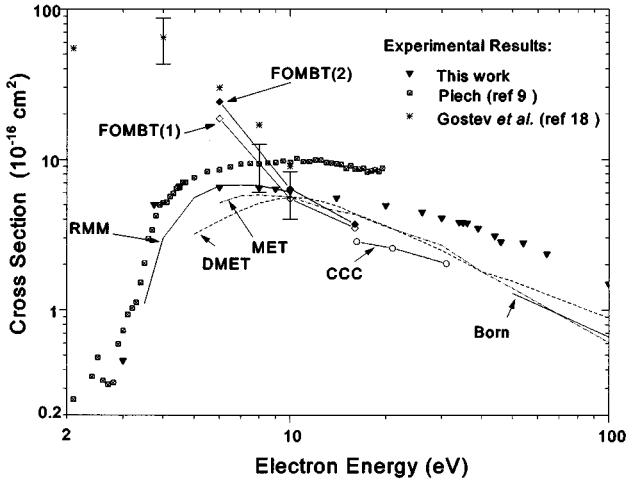

FIG. 12. Comparison of three sets of experimental cross sections (represented by individual data points) for excitation out of the $2\ ^3S$ level into the $3\ ^3D$ level with seven sets of theoretical values (represented by curves). The total experimental uncertainty for the present work and for Ref. [9] is indicated by an error bar on one data point. The error bar associated with the data point of Ref. [18] is taken from that paper. Most of the theoretical curves are obtained by joining the values at different energies given in the original papers.

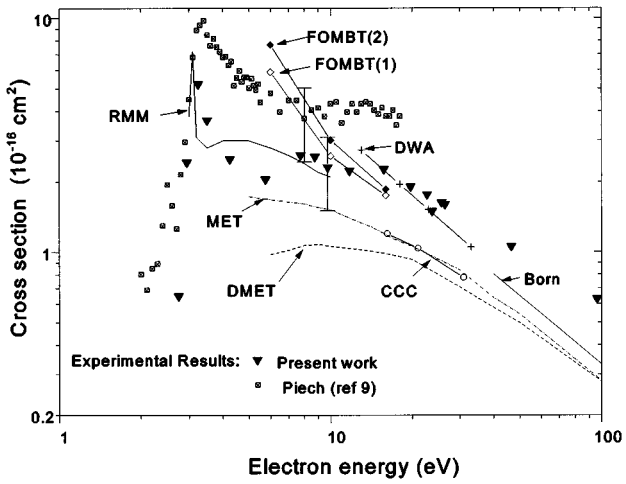

FIG. 13. Comparison of two sets of experimental cross sections (represented by individual data points) for excitation out of the $2\ ^3S$ level into the $3\ ^3S$ level with eight sets of theoretical values (represented by curves). The total experimental uncertainty for each set of experimental data is indicated by an error bar on one data point. Most of the theoretical curves are obtained by joining the values at different energies given in the original papers.

cross sections out of the $2\ ^3S$ level of Ref. [27], and correspondingly, the integral cross sections for excitation out of the $2\ ^3S$ level calculated by the DWA, and, to a lesser extent, the FOMBT (except the low-energy part), come closer to our experimental cross sections than do the CCC values for these integral cross sections.

Our $2\ ^3S \rightarrow 3\ ^3P$ excitation data cover only two energies. At 10 eV our cross section, in units of 10^{-16} cm^2, is 1.6, which is again quite close to the RMM value of 1.8, larger than the MET and DMET values (0.618 and 0.97), and smaller than the two FOMBT values (2.30 and 2.90). Of the theoretical calculations cited above, only the CCC includes cross sections for the 4^3D level which are 0.513, 0.497, and 0.429 at 16.2, 21, and 31 eV, respectively, as compared to the corresponding values of 0.93, 0.86, and 0.73 from our experiment.

It should be pointed out that our excitation function (as well as that of the first-generation experiment) for the $3\ ^3S$ level shows a narrow peak at 4 eV preceding the broad main curve. This feature of a double maximum is also found in the RMM calculation.

VI. CONCLUSIONS

We have used a fast metastable He atomic beam target for studying electron-impact excitation out of metastable levels by using charge exchange between He^+ ions and Cs atoms. Because of the near-energy resonance the He atoms formed in this reaction are mostly in the metastable levels with only a small percentage ($\sim$10%) of the atoms in the ground level. This is a significant improvement over the metastable atom target used in the first-generation experiments in which the metastable atoms are produced in a hollow cathode discharge with a density ratio of a few parts in 10^5 ground-state atoms. Because of this very low concentration of metastables from the hollow cathode discharge, the earlier measurements of excitation cross sections out of the metastable levels were limited to electron energies below the threshold of ground-level excitation. Using the new metastable atom target we have measured excitation cross sections out of the metastable levels up to 500 eV. An additional benefit of a fast beam target is the reduced effect of cascades from higher levels.

To obtain absolute cross sections from the intensity of the radiation emitted by the excited atoms, we have measured the spatial distribution of the electron and metastable atom beams, the optical profile of the detection system, as well as measuring the absolute atom beam flux. The motion of the excited atoms is also taken into account since the target atoms are moving at velocities in the range of 3×10^7 cm/s, the distances the atoms can travel in one lifetime are comparable to the size of our viewing region. Because of the very low target density, extreme care is taken to reduce the noise level.

The absolute cross sections from this experiment are smaller than those from the first-generation experiment. On the other hand, the relative cross sections determined by the two experiments agree very well with each other in the energy range where the two sets of measurements overlap. Furthermore, the ratio of cross-section results (i.e., $3\ ^3S$ to $3\ ^3D$) are also in agreement between the two experiments, the absolute results only differ in magnitude by a constant factor. The absolute calibration of the first-generation experiment was done by an entirely different method, i.e., a laser-induced fluorescence (LIF) measurement to give the ratio of the excitation cross section to the known oscillator strength of the $2\ ^2S \rightarrow 3\ ^3P$ transition. This LIF measurement for absolute calibration is being reexamined in order to understand the discrepancy in the absolute cross section, although the two sets of results overlap within their limits of uncertainty.

Theoretical calculations of the $2\ ^2S \rightarrow n\ ^3L$ excitation

cross section at low energies have been made by means of a variety of sophisticated theoretical methods. We compare our low-energy cross sections to theoretical calculations, and find good agreement with the R-matrix calculation. In the R-matrix calculation, the 11 lowest states of He ($1\,^1S$, $2\,^3S$, $2\,^1S$, $2\,^3P$, $2\,^1P$, $3\,^3S$, $3\,^1S$, $3\,^3P$, $3\,^3D$, $3\,^1D$, $3\,^1P$) are included. It would be interesting to ascertain whether inclusion of additional states in the close-coupling manifold would significantly affect the calculated $2\,^3S \rightarrow 3\,^3L$ excitation cross sections. Most of the other theoretical calculations are lower than the measured cross sections reported here. A similar discrepancy between theory and experiment generally exists in comparing experimental results for the ionization of metastable helium [26] with theoretical calculations [24,28], as well as in the measured differential cross sections for metastable helium [27] and theoretical values [15,21–24,29]. One exception to this general trend is the good agreement with the DWA calculation [21] in the differential and integral cross sections for excitation into the $3\,^3S$ state. Some of the theoretical values cited above were published only very recently. Continued theoretical and experimental efforts on excitation out of metastable states should be most fruitful.

Our high-energy data show that the cross sections have not reached the Born regime even at 500 eV. To make contact with the Born-Bethe theoretical description, measurements must be made in the keV energy range. Efforts to improve the sensitivity of the cross-section measurement are most important toward extending the experiment to high energies as well as obtaining cross sections for excitation into the higher levels.

ACKNOWLEDGMENTS

This work was supported by the National Science Foundation. The authors wish to thank G. A. Piech for providing us with his measured $2\,^3S \rightarrow n\,^3L$ direct cross sections. We are also grateful to R. B. Lockwood, C. M. Martin, and M. A. Eriksson for some initial assistance in constructing the apparatus.

[1] J. Franck and G. Hertz, Ber. Dtsch. Phys. Ges. **16**, 512 (1914).
[2] C. C. Lin and L. W. Anderson, Adv. At. Mol. Opt. Phys. **29**, 1 (1992).
[3] S. Trajmar and J. C. Nickel, Adv. At. Mol. Opt. Phys. **30**, 45 (1993).
[4] R. M. St. John, F. L. Miller, and C. C. Lin, Phys. Rev. **134**, A888 (1964).
[5] D. W. O. Heddle and J. W. Gallagher, Rev. Mod. Phys. **61**, 221 (1989).
[6] D. L. A. Rall, F. A. Sharpton, M. B. Schulman, L. W. Anderson, J. E. Lawler, and C. C. Lin, Phys. Rev. Lett. **62**, 2253 (1989).
[7] R. B. Lockwood, F. A. Sharpton, L. W. Anderson, and C. C. Lin, Phys. Lett. A **166**, 357 (1992).
[8] R. B. Lockwood, L. W. Anderson, and C. C. Lin, Z. Phys. D **24**, 155 (1992).
[9] G. A. Piech (private communication).
[10] C. Reynaud, J. Pommier, Vu Ngoc Tuan, and M. Barat, Phys. Rev. Lett. **43**, 579 (1979).
[11] V. Sidis, C. Kubach, and J. Pommier, Phys. Rev. A **23**, 119 (1981).
[12] See, for example, J. M. Lafferty, J. Appl. Phys. **22**, 299 (1951).
[13] D. Hammer, Vacuum **28**, 107 (1977).
[14] A. Viehl, M. Kanyo, A. Van der Hart, and J. Schelten, Rev. Sci. Instrum. **64**, 732 (1993).
[15] M. R. Flannery and K. J. McCann, Phys. Rev. A **12**, 846 (1975).
[16] K. A. Berrington, P. G. Burke, L. C. G. Freitas, and A. E. Kingston, J. Phys. B **18**, 4135 (1985).
[17] A. A. Mityureva and N. P. Penkin, Opt. Spektrosk. **66**, 1220 (1989) [Opt. Spectrosc. (USSR) **66**, 710 (1990)].
[18] V. A. Gostev, D. V. Elakhovskii, Yu. V. Zaitsev, L. A. Luizova, and A. D. Khakhaev, Opt. Spektrosk. **48**, 457 (1980) [Opt. Spectrosc. (USSR) **48**, 251 (1980)].
[19] D. Ton-That, S. T. Manson, and M. R. Flannery, J. Phys. B **10**, 621 (1977).
[20] Y.-K. Kim and M. Inokuti, Phys. Rev. **181**, 205 (1969).
[21] K. C. Mathur, R. P. McEachran, L. A. Parcell, and A. D. Stauffer, J. Phys. B **20**, 1599 (1987).
[22] E. J. Mansky and M. R. Flannery, J. Phys. B **25**, 1591 (1992).
[23] D. C. Cartwright and G. Csanak, Phys. Rev. A **51**, 454 (1995).
[24] I. Bray and D. V. Fursa, J. Phys. B **28**, L197 (1995).
[25] D. V. Fursa and I. Bray, Phys. Rev. A **52**, 1279 (1995).
[26] A. J. Dixon, M. F. A. Harrison, and A. C. H. Smith, J. Phys. B **9**, 2617 (1976).
[27] R. Müller-Fiedler, P. Schlemmer, K. Jung, H. Hotop, and H. Ehrhardt, J. Phys. B **17**, 259 (1984).
[28] I. R. Taylor, A. E. Kingston, and K. L. Bell, J. Phys. B **12**, 3093 (1979).
[29] A. Franca and F. J. da Paixão, J. Phys. B **27**, 1577 (1994).